

# Chapter 3

## 3. The Teleseismic Tomography Method

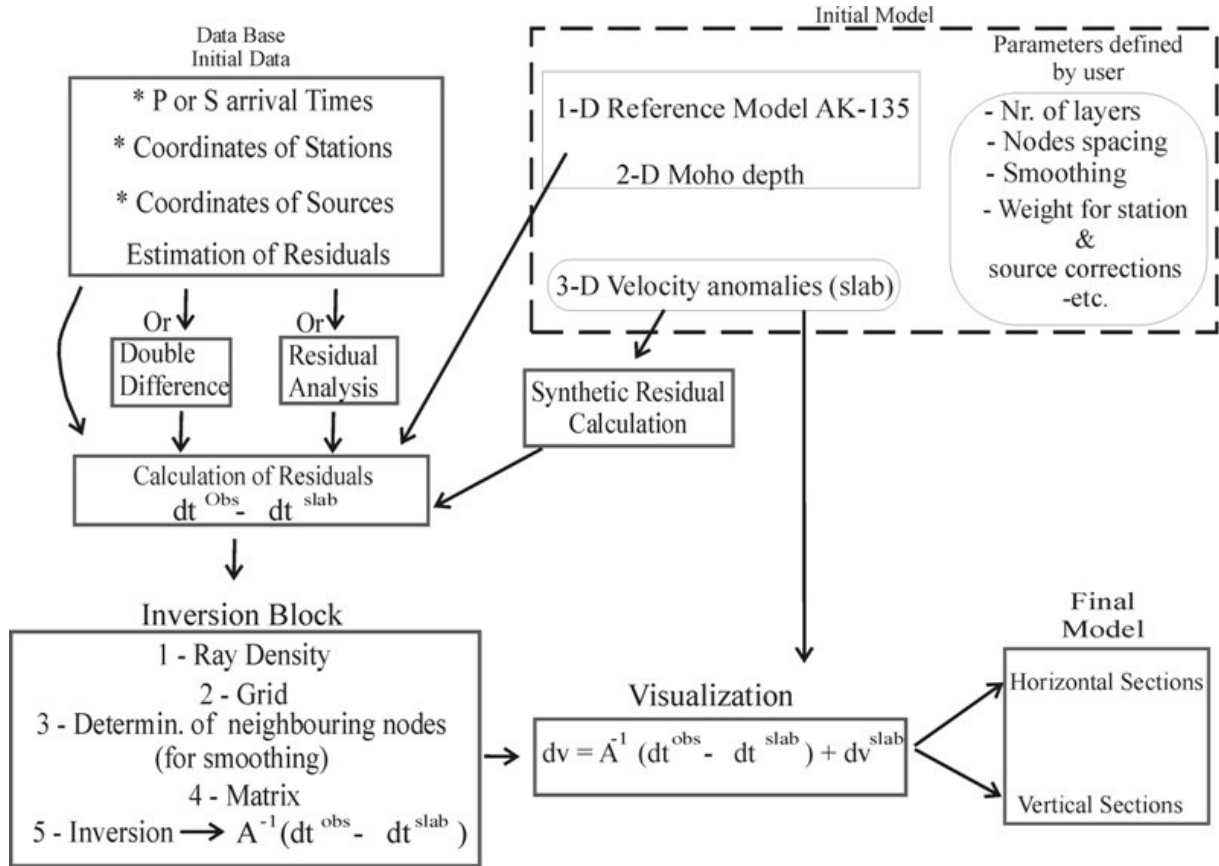
### 3.1. The tomographic inversion method

In geophysics, the earth can usually be described as a first approximation as an onion divided into layers whose properties (e.g. thickness, temperature and density) are responsible for other characteristics (e.g. wave propagation velocity). The number of layers for a given earth model depends upon the assumed structure of the crust, mantle and core discontinuities. There are different types of earth models that can predict the propagation of waves throughout the earth very accurately (e.g. PREM, iasp91, AK-135) and help us to produce a map that images the internal structure of the earth based on velocity variations. Calculating a travel-time anomaly relative to a reference symmetric earth model gives seismologists the possibility of detecting velocity perturbations for particular regions. One of these approaches is named *tomography* after the medical method of Computerized Tomography (CT scan) used to investigate the nature of human bodies. The word “*tomo*” from the Greek “section or slice” has been used to describe a method in which a slice from a three-dimensional (3-D) object provides information about its two-dimensional (2-D) properties. By combining many of these 2-D slices we obtain a 3-D model of the object in question (Lee and Pereyra, 1993)

Teleseismic tomography is a method that provides information about deep seismic velocity anomalies beneath a selected region based on the relative delays of seismic rays arriving from remote events at the stations located in the study area (Figure 2.1). This approach was developed in the seventies (Aki and Lee, 1976; Aki et al, 1977; Aki, K., 1993.) and has since been applied successfully to many different regions (e.g. Achauer, 1992; Evans and Achauer 1994; Koulakov et al., 1995; Wittlinger et al., 1998 and others). The first step in seismic tomography is to formulate the linearized iterative inverse problem by selecting an initial model and the parameters to describe its perturbations and tracing seismic rays through the model for given source-receiver pairs. One method uses an initial model which is a stack of homogeneous flat layers. The model parameters are the perturbations of velocities (or slowness) of the rectangular blocks into which each layer is divided. The lateral size of the model blocks is dependant upon the station spacing of the array (Aki, 1993).

In this study, we followed the same approach of teleseismic inversion as described in Koulakov et al., (2005) to investigate the mantle structure beneath the Dead Sea region. However, some peculiarities of the observation system, configuration and high contrast of the expected velocity anomalies under the Andes required some modifications to the algorithm (see Section 3.2).

The following flow chart portrays the design logic or the connection of the algorithm components and the successive steps that we have used in this process. Different items according to their characteristics (Data Base, Initial Model, Inversion Block, etc.) and their interrelations are also shown (*see diagram below and Appendix A.3.*).

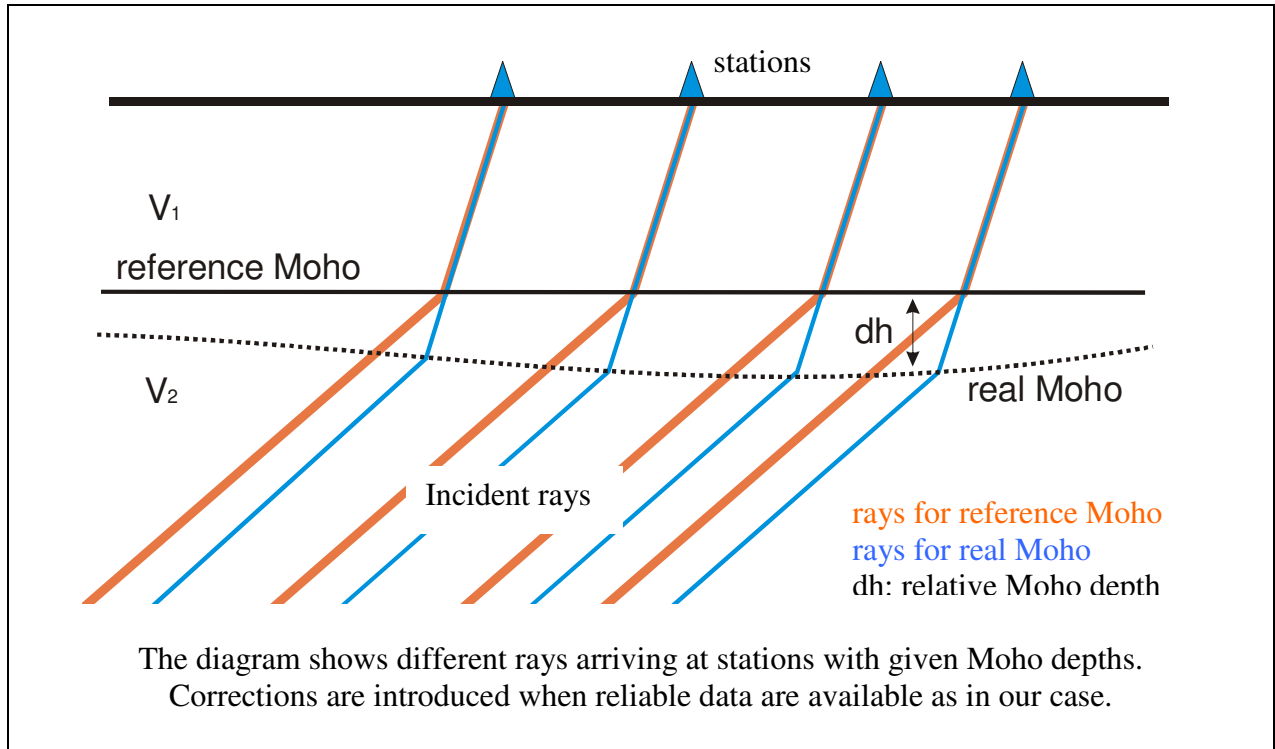


### 3.2. Tomographic inversion: Altiplano

As a preliminary step, the travel-times at teleseismic distances between  $30^\circ$  and  $95^\circ$ , with possibly equal step of epicentral distances are computed according to the 1D Earth model AK-135 (Kennett et al., 1995) and tabulated, from which reference travel-times of the real rays were computed. The times are corrected for the elevation of the stations above sea level by:

$$dt^{topo} = dh \sqrt{\sigma^2 - p^2}$$

where  $\sigma$  is slowness ( $1/v$ ) in the upper-most layer,  $p$  is the ray parameter and  $dh$  is the altitude of the station above sea level.



If there is information about the Moho depth available, as in the case of our study area, it can also be included as an additional correction:

$$dt^{moho} = dh \left[ \sqrt{\sigma_1^2 - p^2} - \sqrt{\sigma_2^2 - p^2} \right]$$

where  $\sigma_1$  and  $\sigma_2$  are the values of slowness under and above the Moho interface,  $p$  is the ray parameter (horizontal component of the slowness vector), and  $dh$  is a relative Moho depth at the entry point with respect to the average crustal thickness in the reference model. In our case, for both profiles along  $21^\circ$  S and  $25.5^\circ$  S, the Moho depth is taken from receiver function data (Yuan et al., 2000). Figure 3.1B shows the Moho depth along the Altiplano profile at  $21^\circ$  S.

We do not consider the correction for the ellipticity of the Earth because the size of the study area is quite small and the ellipticity correction at all stations for one source is practically the same. It could in any case, be included in the source correction term which is obtained during the inversion step. The difference in the ellipticity corrections between the eastern and western-most stations is estimated to be below 0.01s (less than the accuracy of our phase picking) and is

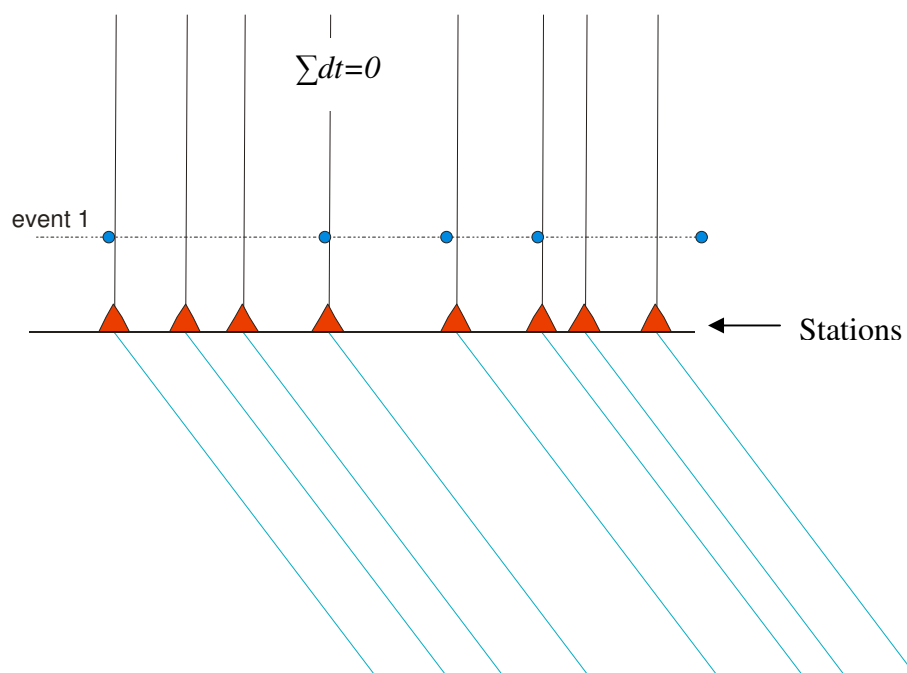
included as a constant in the source corrections (see page 31).

The preliminary values of the residuals are obtained by a simple subtraction of the reference and observed travel-times. Usually, for each event, these residuals are biased due to a number of different factors: mislocation and wrong origin time of source, seismic anomalies along the ray path outside the study area, ellipticity of the Earth, non-accuracy of the reference model, etc. Most of these factors affect the travel-times in the same way from one source (e.g. anomalies in the lower mantle that are assumed to be of the same dimension than the study area), therefore the preliminary source correction is computed to provide a zero value for all residuals:

$$dt_{srce}^0 = \sum_{n=1}^N (dt_n) / N$$

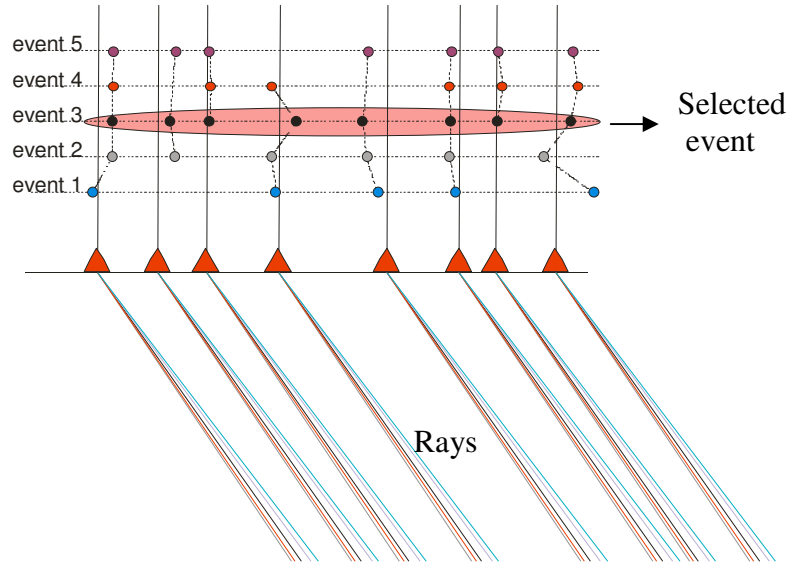
In the next step of residual processing, the source and station corrections are evaluated so that the difference between residuals corresponding to the rays with similar back azimuth and incidence angle recorded at one station were similar. The residuals that do not fit this condition were rejected as outliers. The algorithm is illustrated schematically as follows, where each vertical line means  $dt=0$ , to the left of the lines  $dt<0$  and to the right  $dt>0$ :

Step 1 - Residuals for one event are computed so that  $\sum dt=0$

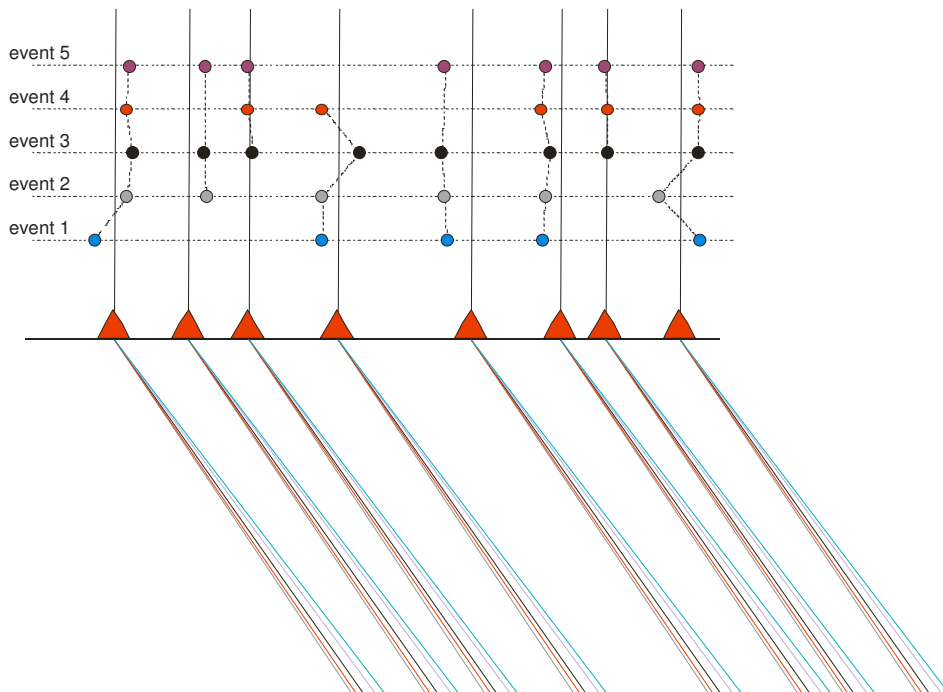


Step 2 - All events providing similar starting parameters are selected. For each event  $\sum dt=0$

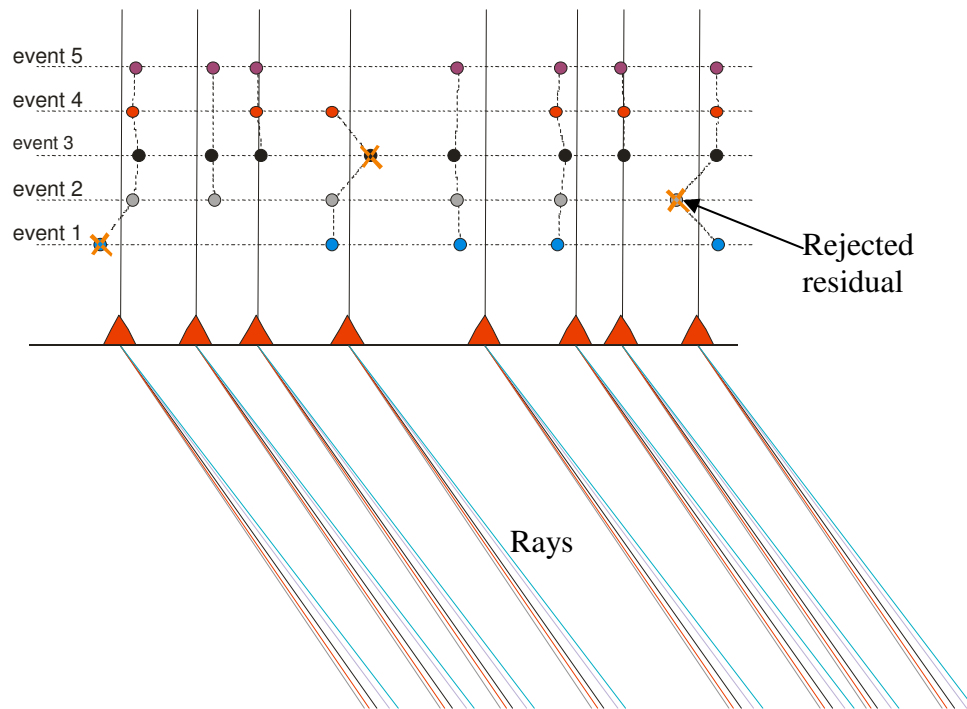
Step 3 - An event with maximal number of records is selected as reference



Step 4 - Source corrections are computed for the other events so that the differential residuals are minimal.



Step 5 - Records with large differential residuals are rejected as outliers.



Step 6 - The procedure is repeated without the outliers

The reason for residuals described as outliers is usually related with problems in the selection of the first arrival of P- and S- waves. Other problems that influence the aspect of the residuals can be associated with timing errors due to low GPS coverage or the presence below the station of local anomalies that are not perceived in other neighbouring stations.

Average values of P-residuals for each station after this step and the ray paths of all recorded rays traced down to the depth of 320 km are shown in Figure 3.1A. In the Appendix (A.6.) the entire set of residuals is presented without the corrections according to their different back-azimuths.

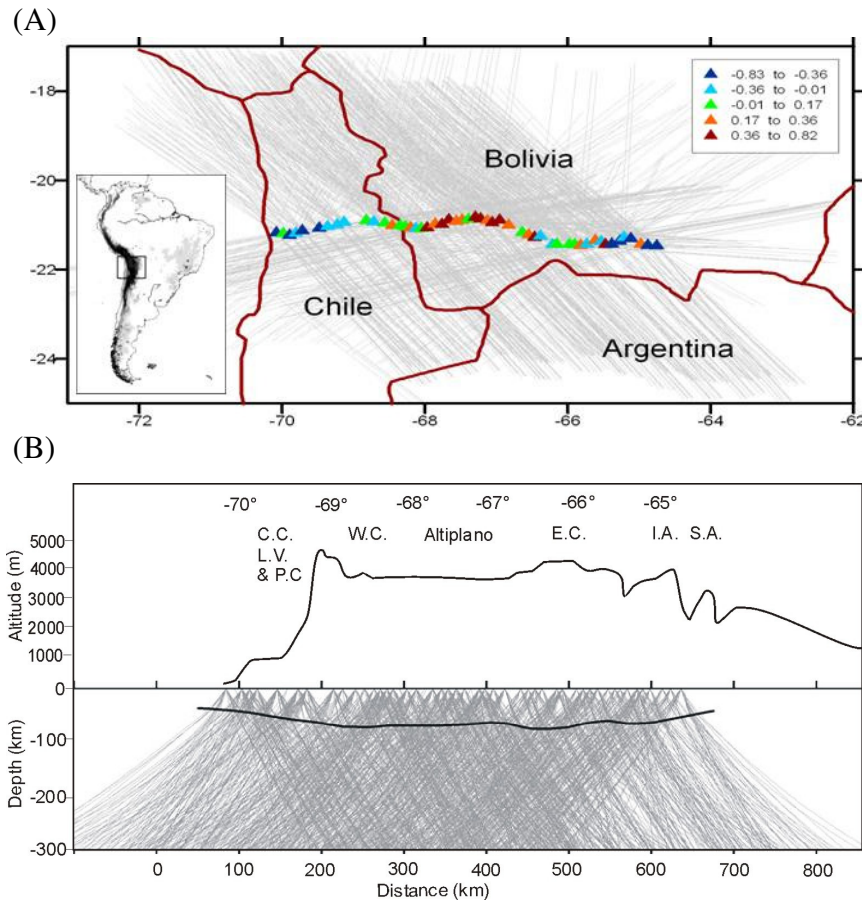


Figure 3.1: Configuration of the Altiplano seismological profile. (A): Map of the station distribution along 21°S. The colour scheme indicates the values of average residuals at the stations after corrections for topography and Moho discontinuity; positive residuals (red triangles) correspond to areas of low seismic velocities, negative residuals (blue triangles) correspond to high seismic velocities; ray paths down to 350 km are shown by grey lines. (B): Projection of the ray paths onto a vertical profile with an exaggerated topography scale along the stations profile. Morphological units along the profile are: C.C.: Coastal Cordillera; L.V.: Longitudinal Valley; P.C.: Precordillera; W.C.: Western Cordillera; E.C.: Eastern Cordillera; IA: Interandean and S.A.: Subandean. The bold black line in the vertical section shows the Moho depth (Yuan et al., 2000) used in this study to correct the residuals.

The resulting velocity model was computed in nodes of a parameterization grid distributed in the study volume according to the ray density. For the P- wave model, the uppermost level of the study volume was defined from 20 km as the minimum depth that is where a sufficient number of ray intersections between neighbouring stations occur. The bottom limit was fixed to 320 km depth, which is compatible with the length of the profile. The parameterization nodes consisted of 10 horizontal planes located at depth steps of 30 km. Examples of the grid construction according to the ray density at various depth levels are shown in Figure 3.2. To avoid an excessive concentration of nodes in the area of ray fluctuations, we fixed the minimal distance between the nodes at 25 km. Velocity distribution between nodes is defined using a bilinear

interpolation method. The number of nodes at each level depends upon the value of the fixed minimal spacing and varies from about 70 at the shallowest level to 100 at the deeper levels.

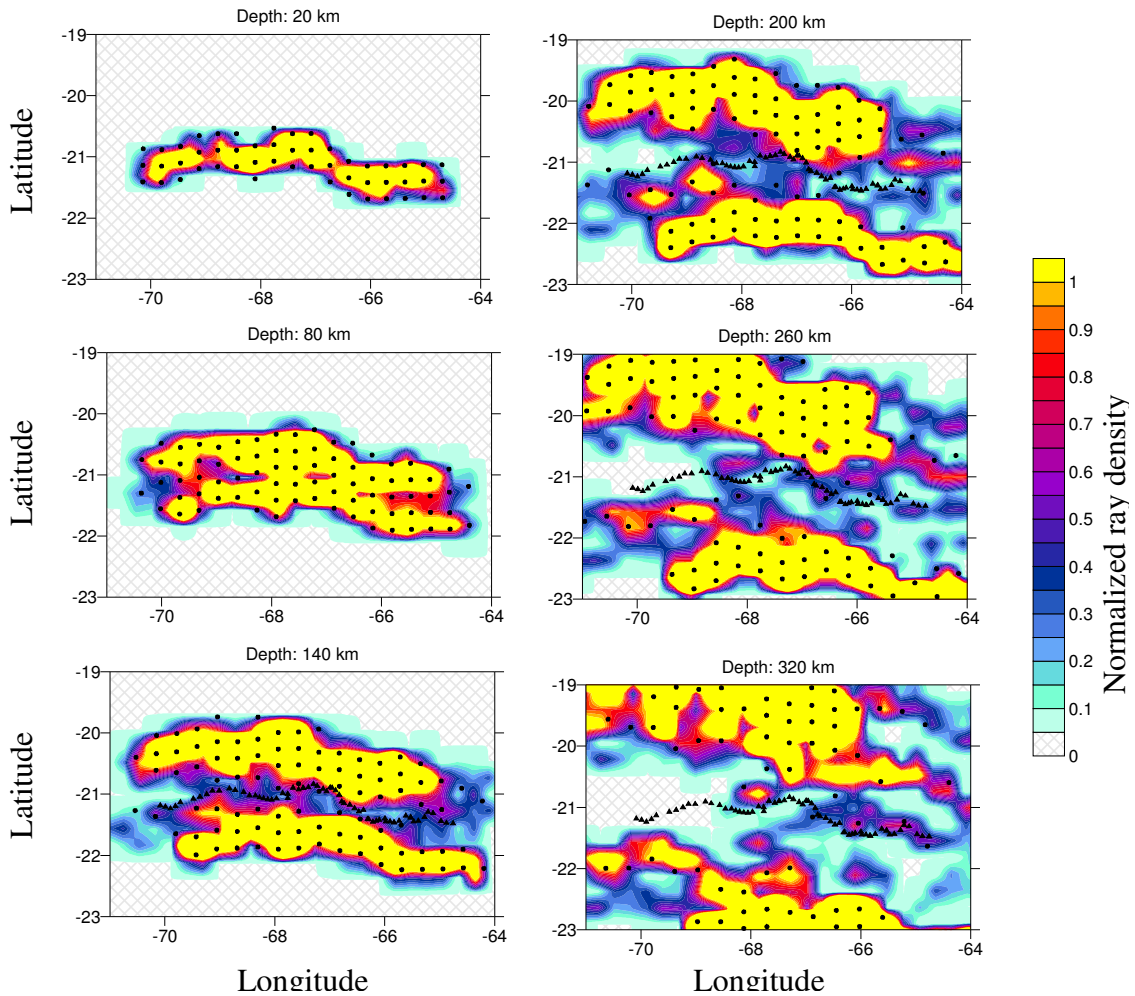
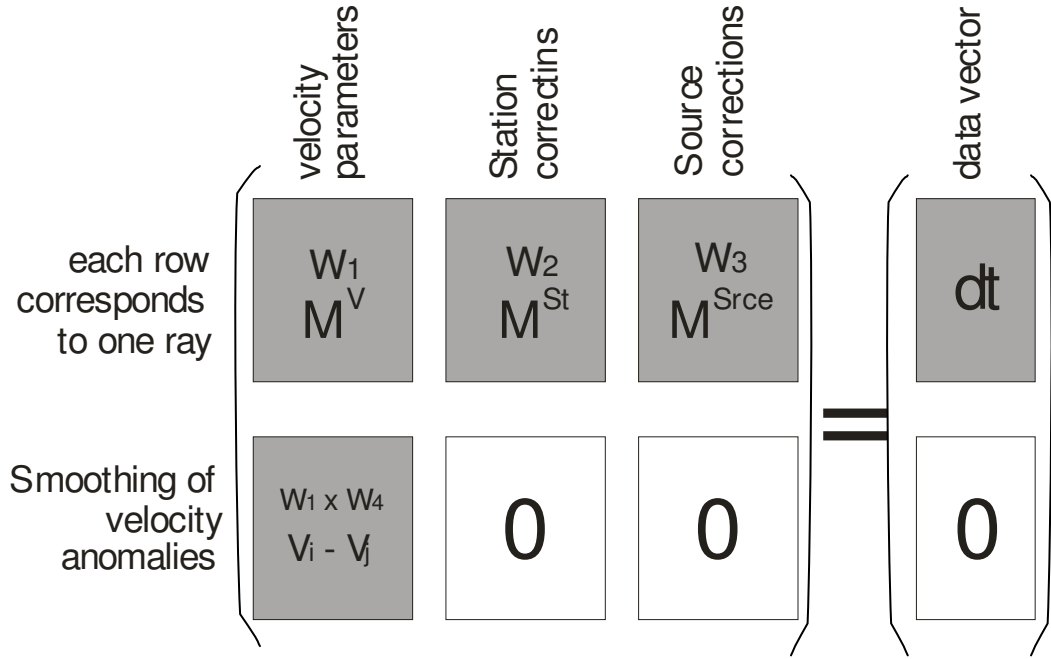


Figure 3.2: Examples of the grid construction according to ray density at various depth levels. Note the influence of the rays for depths greater than 200 km lack the resolution beneath the stations along the profile (Black triangles display the station locations when the rays start to split in their incidence angles from north and south). Colours show normalized values of the ray density.

For the S-wave model, and due to a significantly smaller number of observations, the parameterization grid was sparser than for the P- wave model. The nodes were distributed at 10 horizontal levels down to a depth of 320 km with steps of 30 km. The minimal distance between the nodes was 40 km and the number of nodes varied from 30 at the shallowest plane to 40 in the deepest one.



The structure of the matrix used to determine the velocity field and the source and station corrections is shown in the diagram above. The matrix elements responsible for the velocity variations,  $M^V$ , are computed on the basis of the ray segments located in the study volume. We use the ray paths computed using the 1D spherical-velocity model. For any point of a ray, eight nodes of the parameterization grid are selected, so that they form a parallelogram that contains the current point. Velocity inside the parallelogram is interpolated bilinearly. The elements of the matrix are computed as:

$$M_{ij}^{Vgp(s)} = -\frac{1}{\Delta V_j^{p(s)}} \int_{\gamma_i} \frac{\Delta U_j(s)}{V_0^2(s)} ds$$

where  $i$  is the ray number (row of the matrix),  $j$  is the parameter number (column of the matrix),  $\gamma_i$  is the ray path,  $S$  is a point on the ray,  $\Delta V_j^{p(s)}$  is the unit velocity variation at the  $j$ -th node,  $\Delta U_j(s)$  is the velocity variation at the current point of the ray due to velocity variations at the  $j$ -th node and  $V_0^2(s)$  is the reference velocity at the current point.

An additional block of the matrix allows the regularization of the smoothness of the obtained 3D velocity distribution. Each row of this block contains only two non-zero elements with opposite signs that correspond to parameters in the neighbouring nodes. In this block, the data vector is

assigned zero.

The source corrections,  $M_{srce}$ , include all factors that affect the travel-times between the source and entry point of the study volume; e.g. mislocation and wrong origin time of the source, seismic anomalies along the ray path outside the study area, ellipticity of the Earth, inaccuracy of the reference model, etc. In each row of the matrix, there is one element responsible for the source correction,  $M_{srce}$ , which is constant and equal to 1.

The station corrections include all the unaccounted factors between the station and the upper limit of the study volume: velocity heterogeneities in the crust and in the uppermost mantle, Moho depth, sediments etc. Station corrections are determined using additional elements in every row of the matrix,  $M_{st} = 1$ .

The weight of the different parameters is controlled using four tuning parameters; W1 for the amplitude of the velocity model, W2 for the station correction, W3 for the source corrections and W4 for the tuning of the smoothness of the velocity model. The determination of these parameters is nevertheless an ambiguous and delicate problem. For example, increasing the role of station corrections causes the smoothing of the anomaly amplitudes in the uppermost part of the study area. Varying the source parameters can change velocity distribution in the lower part, although in practice those changes are not dramatic. All of these coefficients are estimated using a-priori knowledge about the expected values of the unknown parameters and the results of the synthetic tests.

### **3.2.1. Synthetic tests: Altiplano**

The synthetic test is a very important step, which is performed in parallel to the real data inversion. By executing a synthetic test, it is possible to explore vertical and horizontal resolutions that provide essential information about the trustworthiness of the features in the final inversion of the real data. On the other hand, synthetic tests also provide optimal estimations of the parameters used for the real data inversion.

Here we present results for two types of tests, namely for horizontal and vertical anomalies, that

aim to reconstruct the presence of realistic anomalies expected in the study area (e.g. intracrustal, lithospheric features and the slab). The synthetic tests are performed using the same geometry (earthquake/stations) as in the case of the real data set.

### 3.2.1.1. Horizontal tests

To check the capacity of the algorithm to reconstruct horizontal anomalies we performed the following tests using different-shape bodies to simulate the anomalies as shown in Figure 3.3. Data without noise is used to check the theoretical capacity of the observation system to reconstruct given anomalies. The anomalies are represented as prismatic bodies maintaining their shapes from the surface to a depth of 200 km

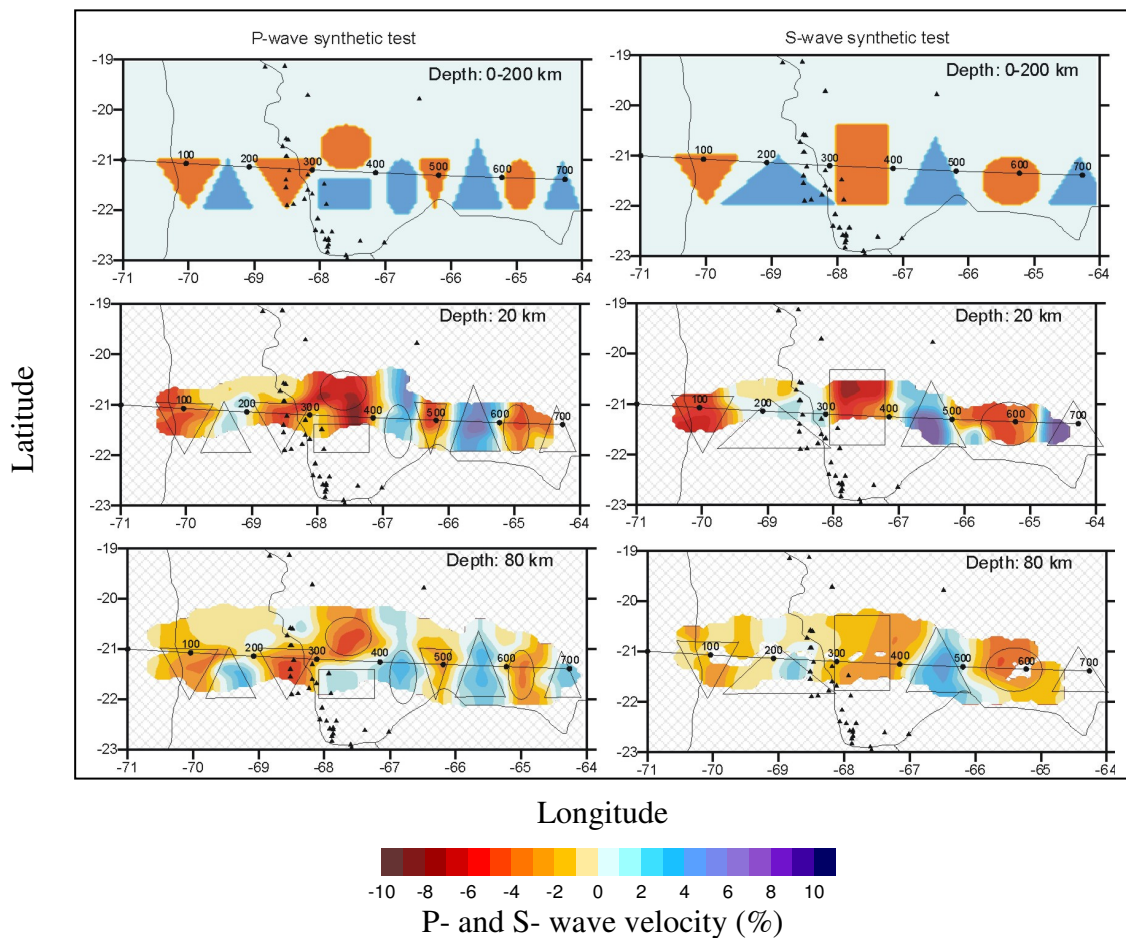


Figure 3.3: P- and S- wave horizontal synthetic anomalies (upper figures) for two depths (20 and 80 km) as an example of the resolution capacity of the algorithm. Inverted red triangles and circles represent low-velocity anomalies in the volcanic arc with amplitude of -4%; blue circles and triangles represent high-velocity units in the fore-arc, Altiplano and Eastern Cordillera with adjoining parts of the Brazilian Shield (+4%). The straight line represents the trace of the profile at  $\sim 21^\circ\text{S}$ . Black triangles are volcanoes and the contour lines are political borders.

The horizontal synthetic tests show that the position of the anomalies can be well reconstructed, but their shapes are not well defined. Some features at both ends of the profile in the upper section (less than ~20 km) are ill resolved due to the absence of incident rays that appear in the successive depth steps. For more examples of synthetic tests see the Appendix where other anomaly shapes are used to evaluate their reconstruction (Appendix A.4.).

### 3.2.1.2. Vertical tests

The initial anomalies in this tests, described in Figure 3.4A, include a slab-shape anomaly with an amplitude of 4% and three crustal anomalies that represent a high-velocity block in the fore-arc (+6%), a low-velocity block of the Altiplano in the centre (-10%) and a high-velocity block in the East which models the position of the Brazilian shield (+4%). The residual times for these tests are computed along the real rays as:

$$dt = \int_{\gamma} \Delta\sigma(\gamma)dS + \tau^{stat} + \tau^{srce} + \varepsilon$$

where  $\Delta\sigma(\gamma)$  is a perturbation of the slowness in the initial synthetic model at a point of the ray,  $\tau^{stat}$  and  $\tau^{srce}$  are the station and source terms, respectively, and  $\varepsilon$  is the random noise. Station and source terms are defined as:

$$\tau_i = ab_i$$

where  $a$  is a constant providing a predefined standard deviation of the corrections and  $b_i$  are random numbers. In our case, we used a periodic repetition of the following seven numbers: 3, -1, 2, -2, 1, -3, 0 which are normalized with a coefficient  $k$  that provides a predefined value of standard deviation for station corrections. The random noise  $\varepsilon$  is produced by a random number generator which provides a statistical distribution similar to that of the real residuals with a predefined average amplitude.

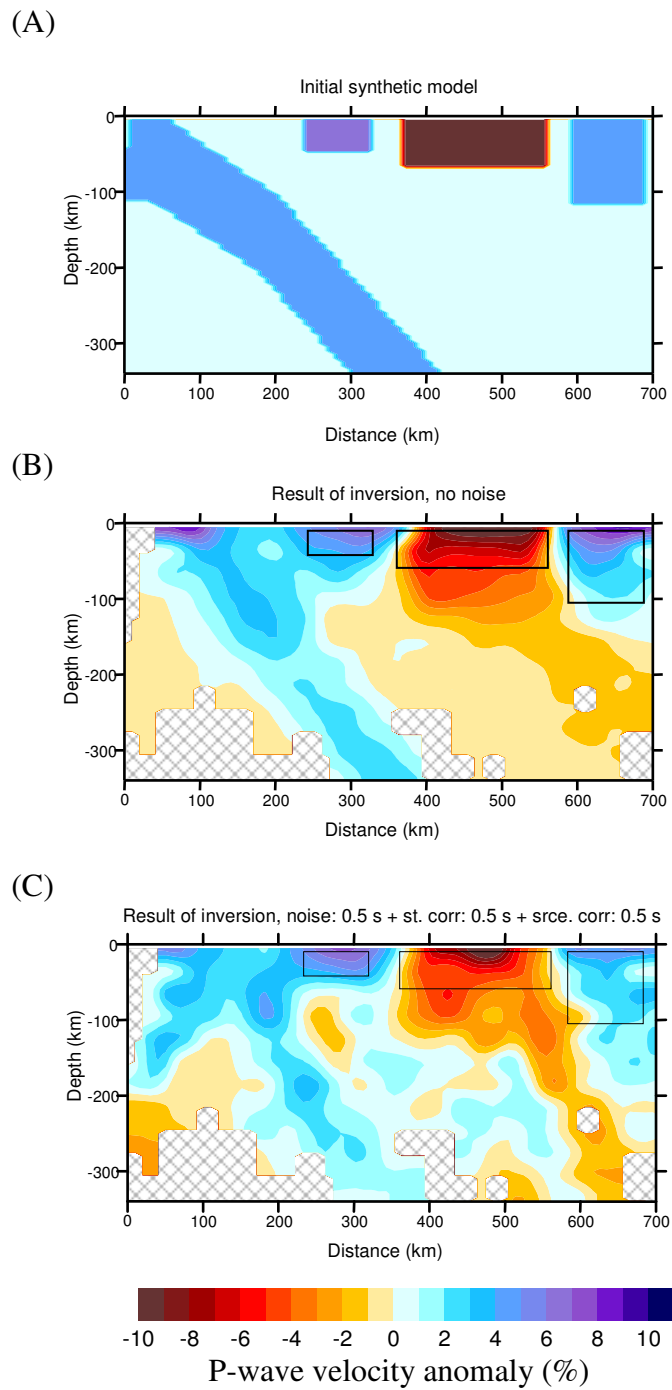


Figure 3.4: Vertical synthetic test showing the results for the reconstruction of synthetic anomalies with rays corresponding to the real data set. (A): Shape of the initial anomalies. (B): Reconstruction using the data without noise. (C): Reconstruction from data with noise. The average noise level is 0.9 s.

Carrying out the inversion without considering noise (Figure 3.4B) shows the algorithm's theoretical capacity to reconstruct the pre-defined shape of the anomalies. In this case, resolution is only limited by the ray coverage and parameterization spacing. This test shows that, despite

the high value of variance reduction, 92%, the teleseismic inversion provides fairly poor vertical resolution, in that not even the noise-free inversion shows a clear lower limit for the crustal blocks due to smearing. Greater vertical smearing is observed towards the eastern boundary of the profile, at depths between 100-300 km. Noisy data and related smearing are shown in Figure 3.3C with noise including station error (0.5 s of deviation), source error (0.5 s) and randomly distributed error (0.5 s). The summary standard deviation of this noise was as large as 0.9 s. Judging from the variance reduction obtained in this test (41%), this noise level is higher than in the real data set (60 % of variance reduction). This means that even a test with lower quality data (41%) than the real data (60%) still provide a reliable reconstruction of anomalies. The horizontal positions of the main anomalies are reconstructed correctly, although the vertical resolution is again disappointing.

### **3.2.1.3. The slab beneath Altiplano**

Due to the poor resolution of the slab in the vertical section, it is necessary to analyze this outcome in detail as it must be considered in the next step of real data inversion. We have the possibility to improve the image of the slab as we use earthquake hypocenters to constrain a realistic shape of the subducted oceanic lithosphere. It should be noted that the slab in the vertical test above was much steeper than what we could observe from the distribution of intermediate depth seismicity in the study region. In the next test we attempt to reconstruct the realistic shape of the slab (Figure 3.5). The initial shape of the slab is shown in Figure 3.5A where the upper surface of the slab is defined as an envelope of the seismicity (hypocenters) located by Engdahl et al. (1998).

The thickness of the oceanic lithosphere was fixed at ~100 km according to a worldwide plot of age versus thickness for oceanic lithosphere from Turcotte and Shubert (1982). The reconstruction of the slab using the data without noise shows the limited capacity of the teleseismic algorithm to reconstruct such kinds of anomalies, which in our case, is strongly shifted upwards (Figure 3.5B). At the same time, the variance reduction after inversion proved to be 97%, meaning that, the initial and reconstructed anomalies provide practically the same values of residuals along the rays used in the data set. This fact can be used to test the effect of the slab anomaly on the interpreted data by reducing the influence of some parameters so that they can be evaluated from independent information during the real data inversion.

Additional vertical and horizontal synthetic tests for the Altiplano profile are presented in the where the results for P- and S- waves are given separately (Appendix A.4.)

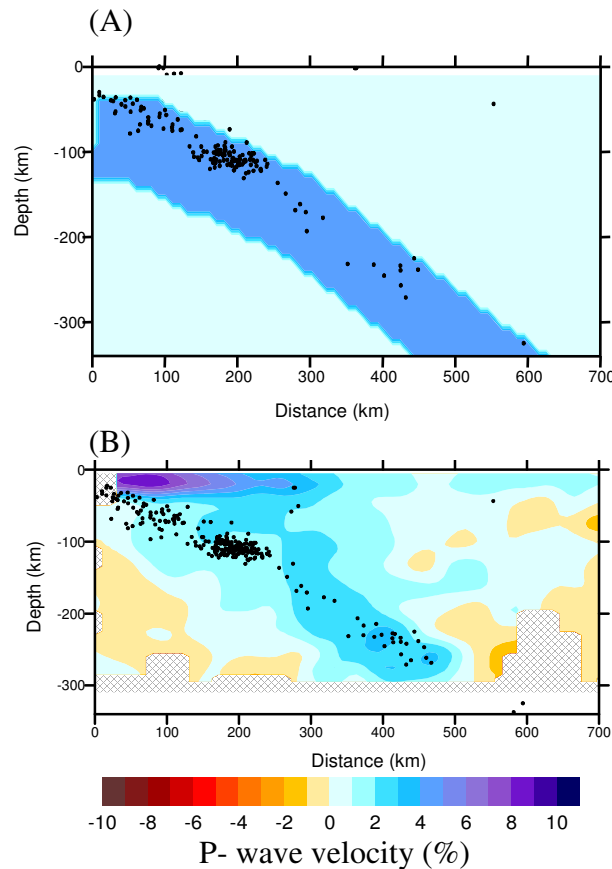


Figure 3.5: Synthetic test showing the poor capacity of the teleseismic approach to reconstruct the real shape of the slab. (A): Initial position of the slab. Earthquake hypocenters are taken from Engdahl et al. (1998). (B): Result of the reconstruction using data without noise, which provides 97% of variance reduction.

It is important to note that the slab, as with any sub-horizontal structure, cannot be reliably recovered. Not all rays reach the receiver by passing through the slab, so that the information about anomalies below, inside and above the slab is confusing. This effect is normally seen in the middle of the slab, where the centre is eviscerated and the ends are well modelled (Figure 3.5B), (Evans and Achauer, 1993).

### 3.2.2. Real data inversion: Altiplano

The poor resolution of the teleseismic inversion for reconstructing the slab-shaped anomaly shown in the previous test suggests that we will be unable to obtain a clear image of the slab from our data set. However, the a-priori information about the position of the slab can be used to

subtract the effect of the slab from the real data inversion. The formalism used to subtract the effect of the slab needs some additional explanations. The possibility of effecting such a subtraction is based on the linearity of the inverse and forward tomographic operators. It is, however, possible to do so if the values of the subtracted anomalies are not too large, so that they do not significantly change the trace of the ray paths. In linear approach, the inversion is performed on the basis of the rays constructed in the reference model (usually a 1D model).

The definition of a linear inversion operator  $A^{-1}$  is:

$$A^{-1}(X+Y) = A^{-1}(X)+A^{-1}(Y). \quad (1)$$

The operator of teleseismic tomographic inversion is assumed linear, so that:

$$dv_1 = A^{-1} dt^{obs} \quad (2)$$

and

$$dv_3 = A^{-1}(dt^{obs} - dt^{slab}) + A^{-1}(dt^{slab}). \quad (3)$$

are equal. The correspondence between  $dv_1 \sim dv_3$  is illustrated in the Figure 3.6 (A and C). If we now apply a direct linear tomographic operator to these two velocity models, we obtain the following residuals:

$$dt_1 = A[dv_1] = A[A^{-1} dt^{obs}] \quad (4)$$

$$dt_3 = A[dv_3] = A[A^{-1}(dt^{obs} - dt^{slab})] + A[A^{-1}(dt^{slab})] \quad (5)$$

which should also be equal; that is  $dt_1 = dt_3$ .

At the same time, in the synthetic test with reconstruction of the slab, we have shown that the variance reduction of such an inversion is 97%. This means that equation 5 may be rewritten as

$$dt^{slab} \sim A(A^{-1} dt^{slab}) \quad (6)$$

with an accuracy of 3%. However, we should note that

$$dv^{slab} \neq A^{-1} dt^{slab} \quad (7)$$

and that due to the poor vertical resolution, the slab is smeared upwards. If instead of the second

term in (3) we use  $dv^{slab}$ , we obtain a new velocity model:

$$dv_4 = A^{-1}(dt^{obs} - dt^{slab}) + dv^{slab} \quad (8)$$

which is obviously not equal to  $dv_2$  (due to the inequality shown in (7)). At the same time, the residuals after application of the direct tomographic operator because

$$dt_4 = A[dv_3] = A[A^{-1}(dt^{obs} - dt^{slab})] + A[dv^{slab}] \quad (9)$$

and are approximately equal to  $dt_2$  in (5) with an accuracy of 3% (97% of variance reduction). This means that three velocity models,  $dv_1$ ,  $dv_2$  and  $dv_3$ , provide similar residuals and therefore can be equally used to explain the observed residuals  $dt^{obs}$ . Since the approximate shape and amplitude of the velocity contrast of the slab present in our study area are known, this information can be used in our starting model. Hence,  $dv_3$  in our case is the most realistic interpretation.

The result of the inversion of the initial observed residuals,  $dv_1$ , according to (2), is shown in Figure 3.6A. The high-velocity anomaly above the earthquake cluster apparently reflects the position of the slab shifted upwards because of the poor vertical resolution, as demonstrated in Figure 3.5. In the Figure 3.6B we present the results of the inversion for the residuals after subtracting the effect of the slab,  $dv^{noslab} = A^{-1}(dt^{obs} - dt^{slab})$ . The amplitude of the P- wave velocity anomaly in the slab was assumed to be 6%. In Figure 3.6C we present the final result which is a combination of the model presented in Figure 3.6B and the initial slab anomaly,  $dv^3$ , according to (3). In Figure 3.6D the model shows the combination of results of inversion for as  $dv^4$  in (8)

Due to the linearity of the inversion operator  $A^{-1}$ , the difference in the residuals produced by the models  $dv_1$  and  $dv_3$  is only related to the difference between residuals computed in the reconstructed and initial slab models shown in Figure 3.5. Because the variance reductions from  $dv_1$  and  $dv_3$  are equivalent, both models can equally be used for explaining the observed residuals. However, the third and fourth models (Figure 3.6C and D) appears to be more reasonable since it takes into account the a-priory position of the slab.

## P-velocity anomalies

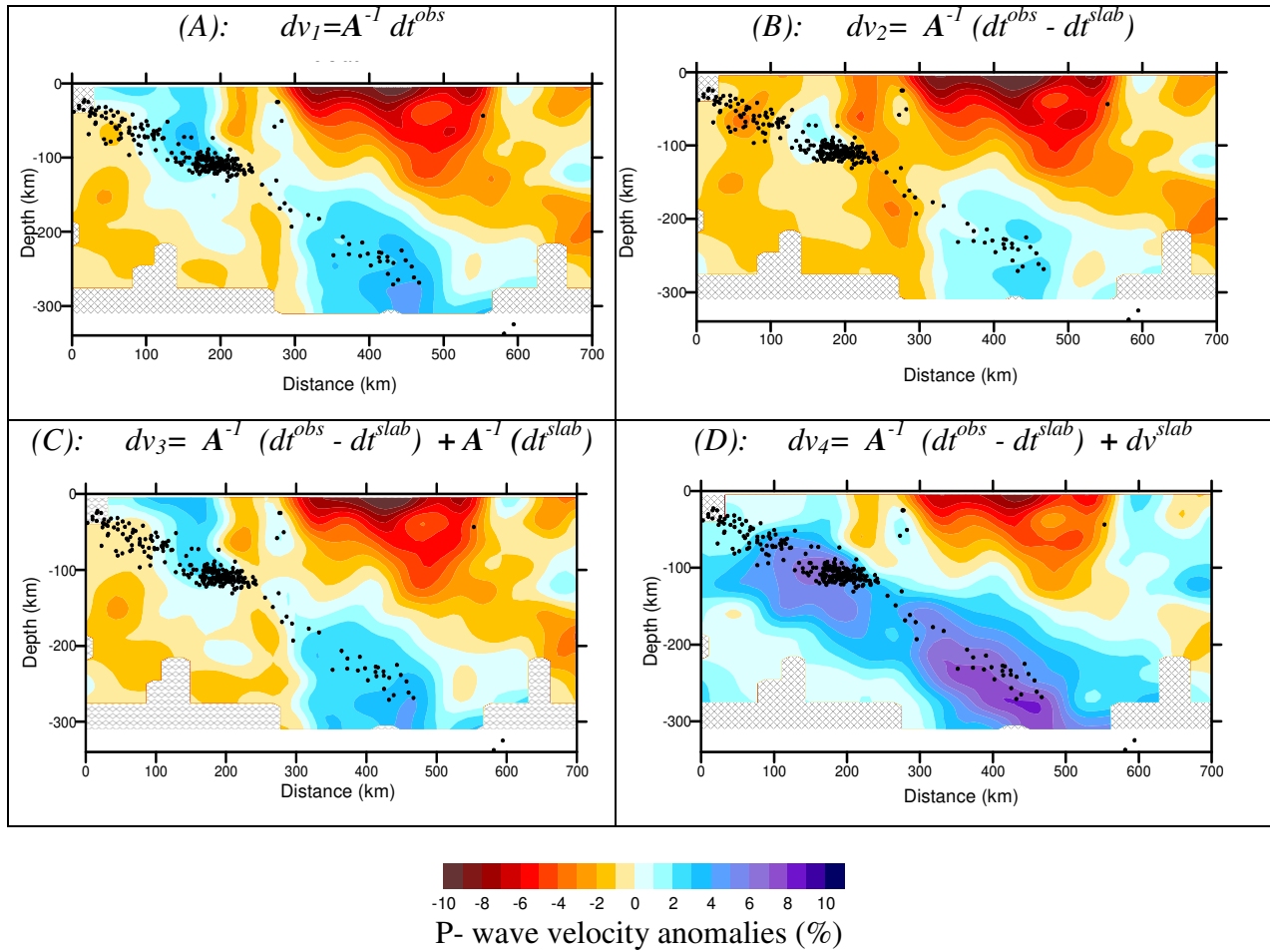


Figure 3.6: Results of the inversion for P-wave residuals with and without a-priori information, presented as vertical sections. (A): Inversion of the observed data for a 1D model. (B): Inversion of the observed data without slab residuals (C): Superposition of the inversion results for “no-slab” residuals with the addition of slab residuals. The models A and C are equivalent when explaining the observed residuals, but C contains a-priori information from the slab. (D): the final section showing the combination of the inversion results for “no-slab” residuals with the model for the slab.

The same strategy as for P- waves was applied for the inversion of the S- wave data. The total number of S- wave residuals (500) was significantly smaller compared to the P- wave data set (1500 rays) and might therefore show a lower resolution. Nevertheless, the results shown in Figures 3.7A, 3.7B and 3.7C, allows us to be optimistic about the reliability of the obtained patterns. As for the P-model, we performed the inversion with and without subtracting the effect of the slab. In the initial model, we used the slab with a velocity contrast of 4%. The results of the P- and S- wave real data inversion are presented as horizontal sections in the Appendix A.5.

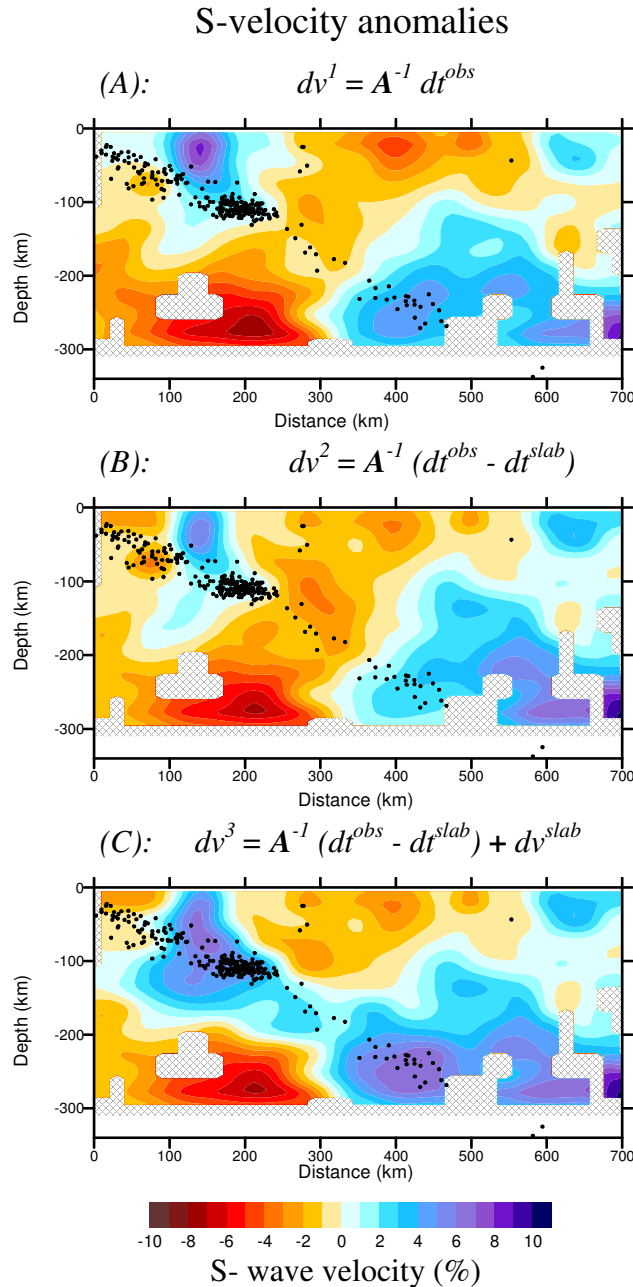


Figure 3.7: Results of the inversion for S- wave residuals with and without a-priori information (vertical sections) using the same strategy as shown in Figures 3.5 and 3.6. The smaller number of detected S- waves is reflected in the poor resolution of anomalies such as the slab. Nevertheless, it is still possible to recognize zones of low-velocity in the upper crust that are not clearly defined by the P- wave inversion.

### 3.3. Tomographic inversion: Puna

The same procedure as for the Altiplano was applied to the southern profile of 19 stations in the Argentine Puna. The stations were corrected for elevation above sea level and Moho depth along the profile. Average values of P-residuals for each station and the ray paths of all recorded rays

traced down to a depth of 260 km are shown in Figure 3.8, (in the Appendix, the residuals are presented without correction according to their back-azimuth – A.6.). The resulting velocity model was computed at the nodes of a parameterization grid distributed in the study volume according to ray density. Digital  $P$ - waveforms from 177 teleseismic events and 29  $S$ -waveforms with  $M_w \geq 5$  were used to obtain the tomographic images.

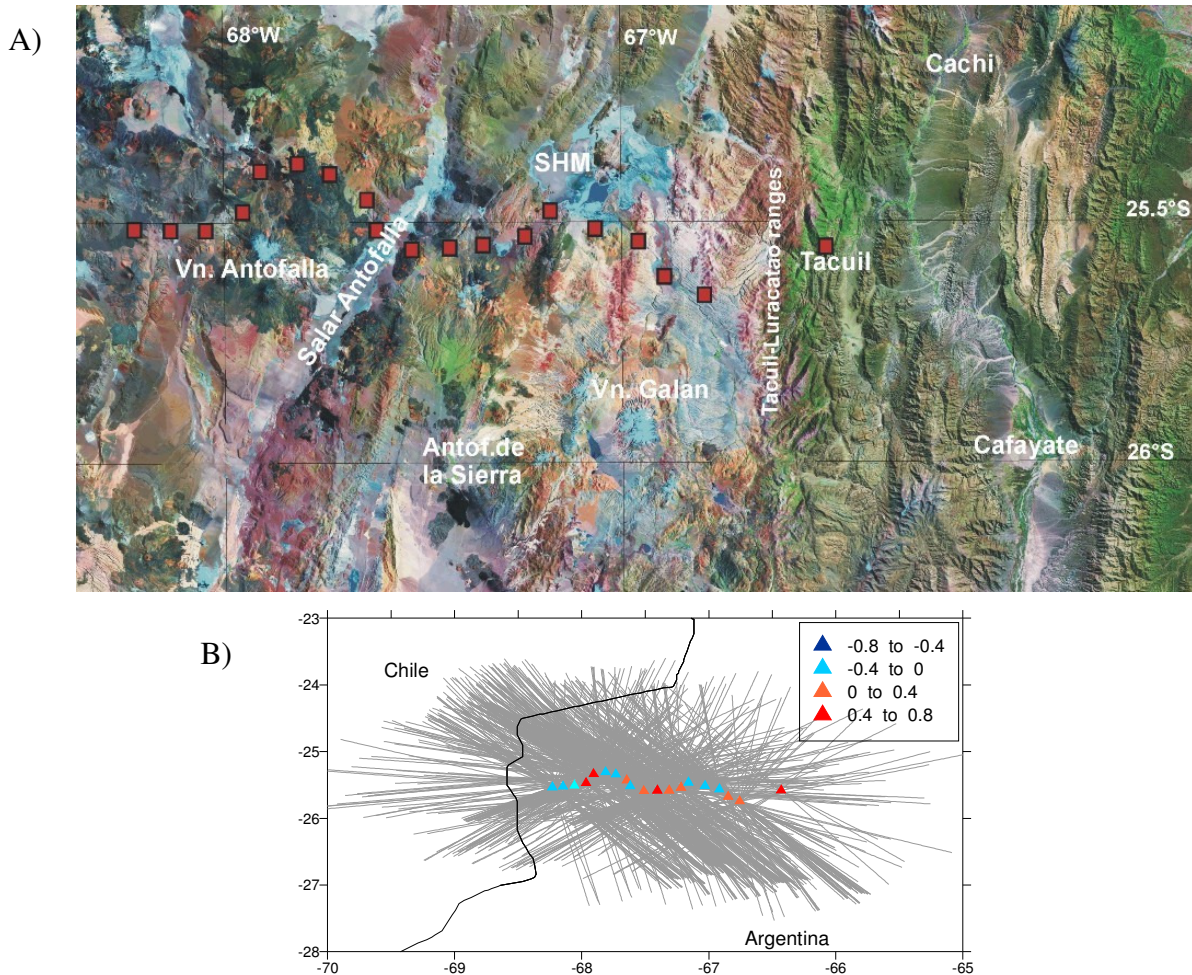


Figure 3.8: A: Landsat image showing the station distribution (red squares) as well as the position of the two prominent volcanic edifices along the profile (Vn. Antofalla and Vn. Galan volcanoes). B: Different colour triangles represent the average-residual values at the stations after corrections for topography and Moho depth; positive residuals (red triangles) correspond to areas of slow seismic velocities and negative residuals (blue) to fast relative velocities; ray paths are indicated by grey lines.

For  $P$ - and  $S$ - wave models, the uppermost level of the study volume was defined at 20 km depth, where sufficient intersections of rays from neighbouring stations are detected, with the lower limit fixed at 200 km depth. The parameterization nodes were constructed at 9 horizontal planes, located at depth steps of 30 km.

Examples of the grid construction according to the ray density at various depths are shown in Figure 3.9. To avoid an excessive concentration of nodes in the area of ray fluctuations, the minimal distance between nodes was fixed at 25 km. Velocity distribution between nodes is defined by bilinear interpolation. The number of nodes at each level depends on the value of the fixed minimal spacing and varies from about 20 at the shallowest level to 80 at the deeper levels. The same procedure was followed for S-wave velocity model.

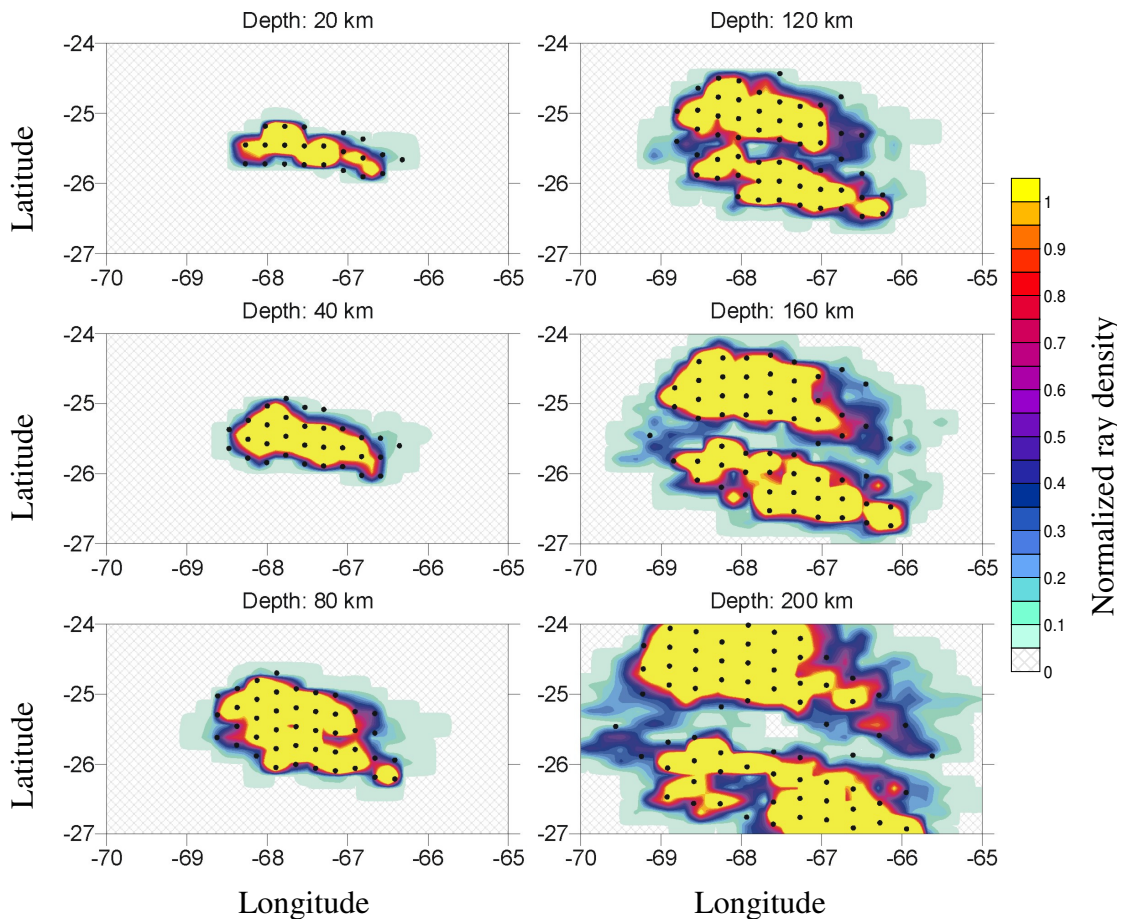


Figure 3.9: Ray density and parameterization grid for Puna profile. Colors show normalized values of the ray density

### 3.3.1. Synthetic tests: Puna

As mentioned before the synthetic tests are very important to explore vertical and horizontal resolutions and provide optimal estimations of the parameters used for the real data inversion. The synthetic tests are performed using the same geometry (earthquake/stations) as in the case of the real data set. The general procedure for the Puna synthetic tests follows that for the Altiplano explained in more detail in section 3.2.1.

### 3.3.1.1. Horizontal tests: Puna

To check the algorithm's ability to reconstruct horizontal anomalies, we performed the following tests using different-shaped bodies to simulate the anomalies, as shown in Figure 3.10. The anomalies are represented by prismatic bodies that conserve their shape from the surface to a depth of 200 km.

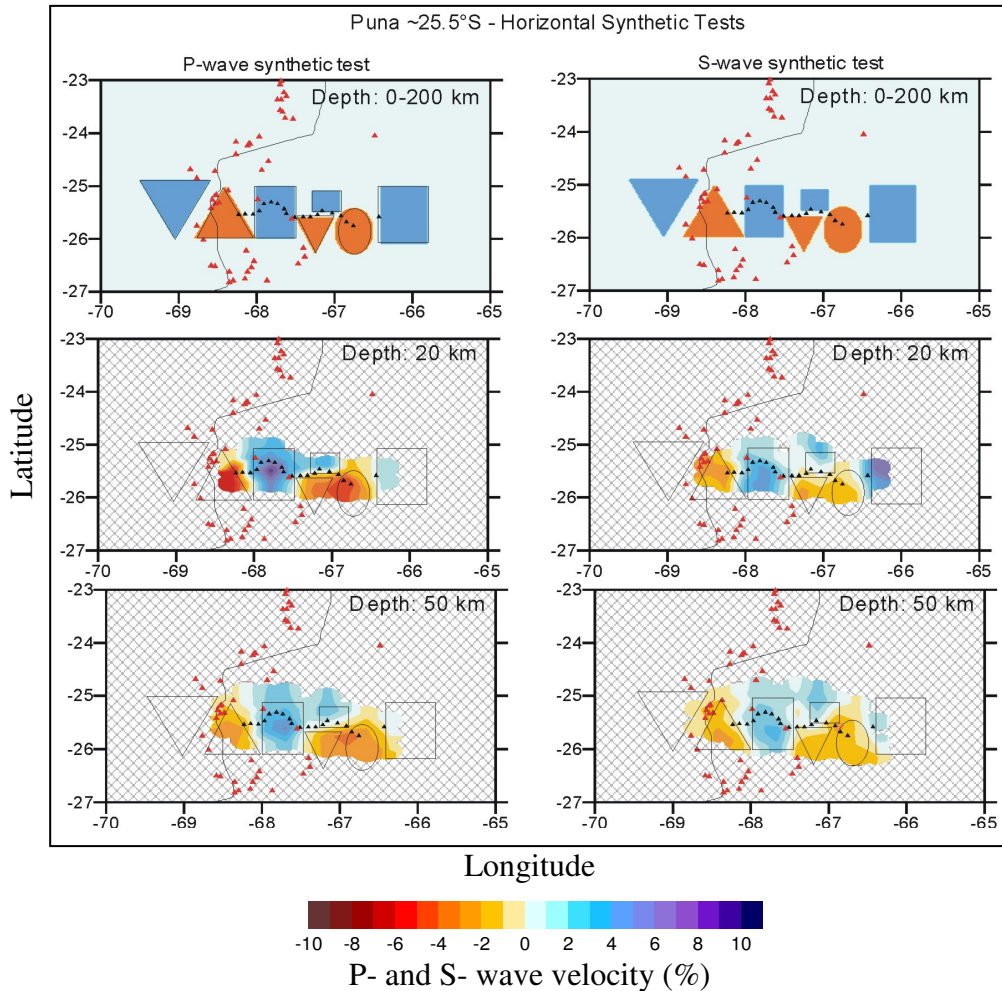


Figure 3.10: P- and S- waves horizontal synthetic anomalies (upper figures) for two depths (20 and 80 km) as an example of resolution capacity of the algorithm. Orange figures (triangles and circles) represent low-velocity anomalies as the volcanic arc with amplitude of -4%; blue squares represent high-velocity units in the fore-arc, Puna plateau and Eastern Cordillera. Black triangles represent stations at  $\sim 25.5^\circ\text{S}$ . Small red triangles are volcanoes. Contour line: political border between Argentina and Chile (see Fig.3.8B).

The synthetic test results show that the position of the anomalies is well reconstructed. The shape of the figures, however, remain not so well constrained, but considering the small number of stations and the length of the profile ( $\sim 200$  km), it is still possible to detect the anomalies at depth. In the upper section, some features that are located at both ends of the profile (west and east) are not resolved due to the absence of incident rays. In this case, it is impossible to make

assumptions about regions in the fore-arc as was done for the Altiplano. For more examples of the horizontal synthetic test see the Appendix A.4.

### 3.3.1.2. Vertical tests

Here we present the results for two tests that are based on real anomalies expected in the area of the Puna profile for P- wave velocity anomalies. The initial anomalies shown in Figure 3.11 include three crustal anomalies that should represent a low-velocity block (-6%) in the volcanic arc, a high-velocity block of the Puna in the centre (+8%), and a low-velocity block in the East which models the presence of some back-arc volcanoes and the eastern border from the plateau (-6%). An additional low-velocity block (-3%) has been included below the crust between 80 km and 150 km depth. The results show that the shapes of the crustal anomalies are well reconstructed and that the smearing is only seen vertically.

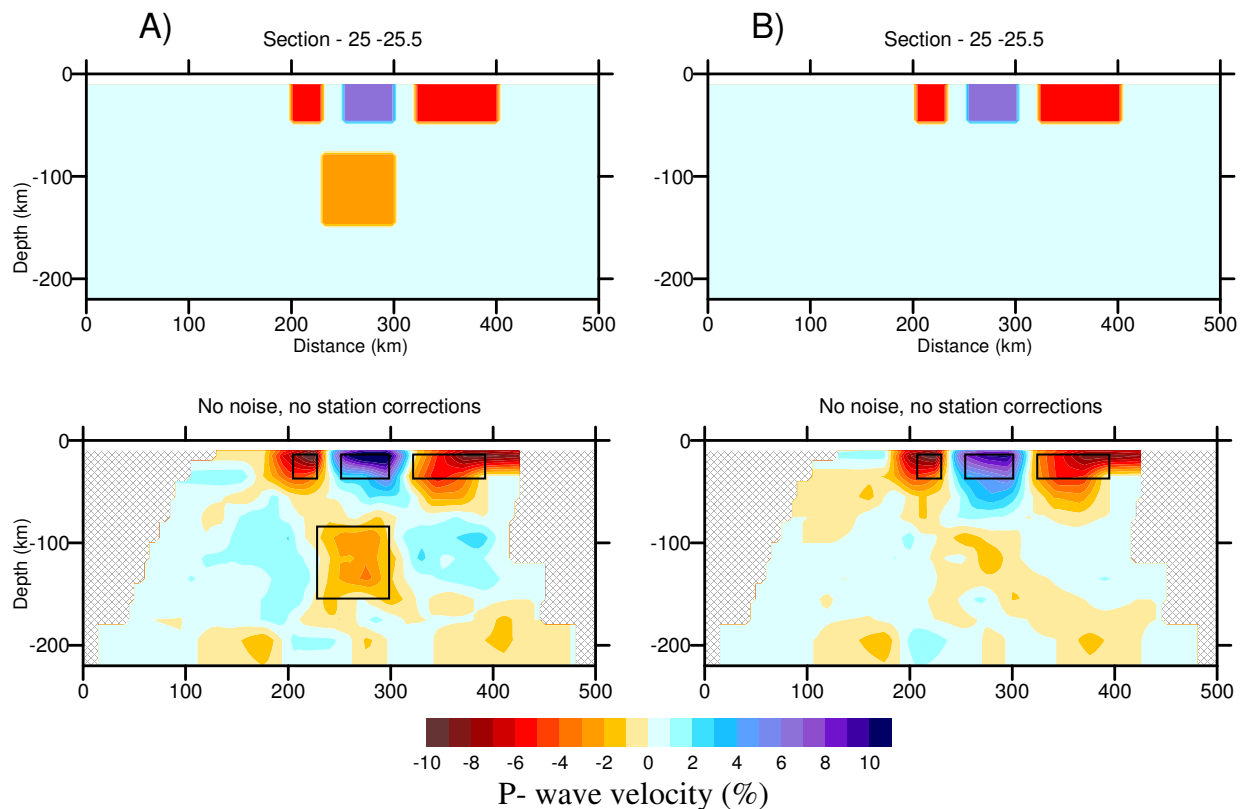


Figure 3.11: Synthetic test for the Puna profile showing the results of the reconstruction of synthetic anomalies with the rays corresponding to the real data set. A): Shape of the initial anomalies, 4 in this case, simulating upper crustal anomalies and an internal anomaly represented as a block between 80 and 150 km. (B): The block anomaly is subtracted from the simulation and reconstruction is made using data without noise and stations corrections. The west-east profile between  $70^{\circ}\text{W}$  (0km) and  $64^{\circ}\text{W}$  (500km) shows the distribution of anomalies at deeper levels according to the ray coverage.

After the first approach shown in Figure 3.11, some changes were introduced to include a slab-shaped anomaly with an amplitude of 4% and just two bigger anomalies instead of the previous three or four anomalies (Figure 3.11). In this case, we have one anomaly in the east, representing the low-velocity CVZ or Western Cordillera where the arc volcanoes are located with an amplitude of -7% and a low-velocity block on the eastern border of the Puna plateau (-5%). This was done to test the proposal that back-arc magmatic activity is related to delamination processes (e.g. Kay et al., 1993 and 1997; Schurr, 2000). Vertical smearing is again present but the horizontal position of the anomalies is well reconstructed (Figure 3.12). For more examples of the vertical synthetic tests see the Appendix A.4.

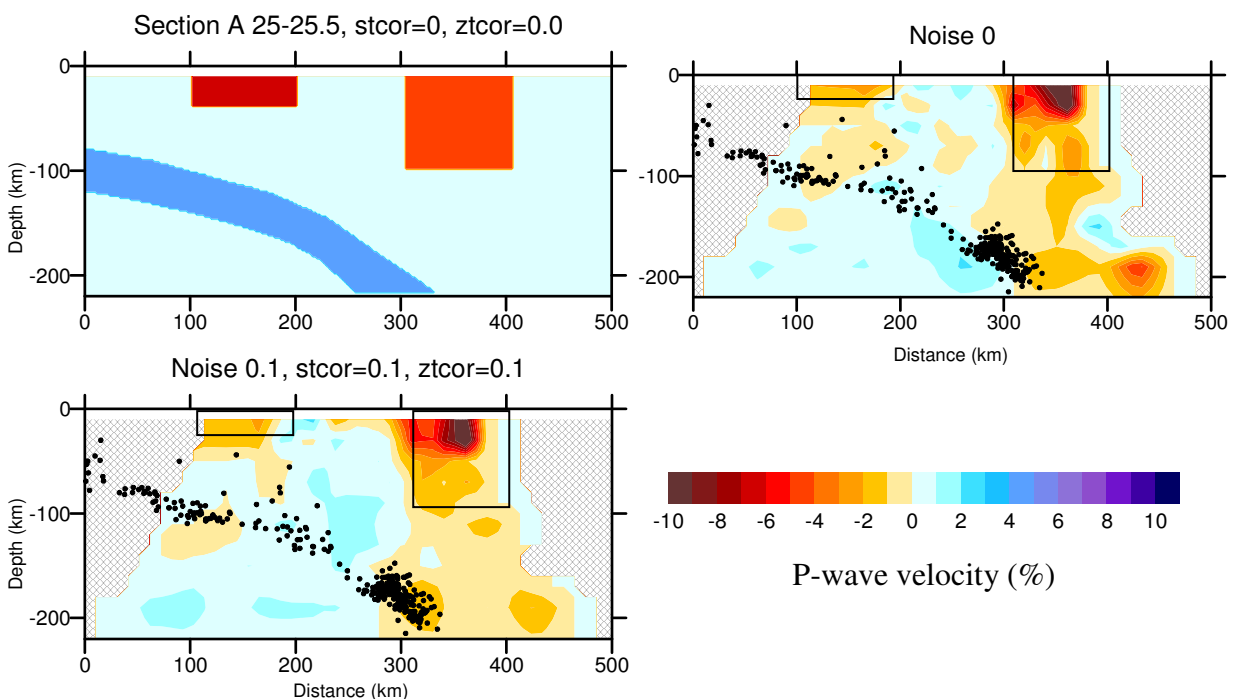


Figure 3.12: Section showing the inferred anomalies for the crust and position of the slab based on seismicity from Engdahl et al. (1998). Note that the smearing arising from using data without noise is strong in the vertical resolution of the eastern block. When applying small amounts of noise, station (*stcor*) and source (*ztcor*) corrections, the smearing is reduced but the anomalies remain in their proper positions. The slab anomaly can not be reconstructed, even when no noise is applied to the model. Colour scale represents relative velocity in %.

### 3.3.1.3. The slab beneath Puna

The image with the position of the slab in Figure 3.12 shows results that this feature is not resolved while the upper-crust anomalies are well reconstructed. The slab's identification needs to be improved and this is done in the following step. As explained in section 3.2.1 (Figure 3.5),

we do not have a good resolution of the slab. At this latitude, the presence and position of the slab has always been a subject of controversy since this is a zone of transition between normal subduction to the north ( $\sim 30^\circ$  is the dipping angle of the slab) and flat subduction ( $\sim 10\text{-}15^\circ$ ) to the south of our study area (Wigger et al., 1991; Cahill and Isacks, 1992; Withman et al., 1996; Allmendinger et al., 1997; Kay and Kay, 1993 and 1994; Kay et al., 1999). Remember that sub-horizontal structures cannot be reliably recovered (Evans and Achauer, 1993). The approach used to image the slab is similar to that introduced in section 3.2.

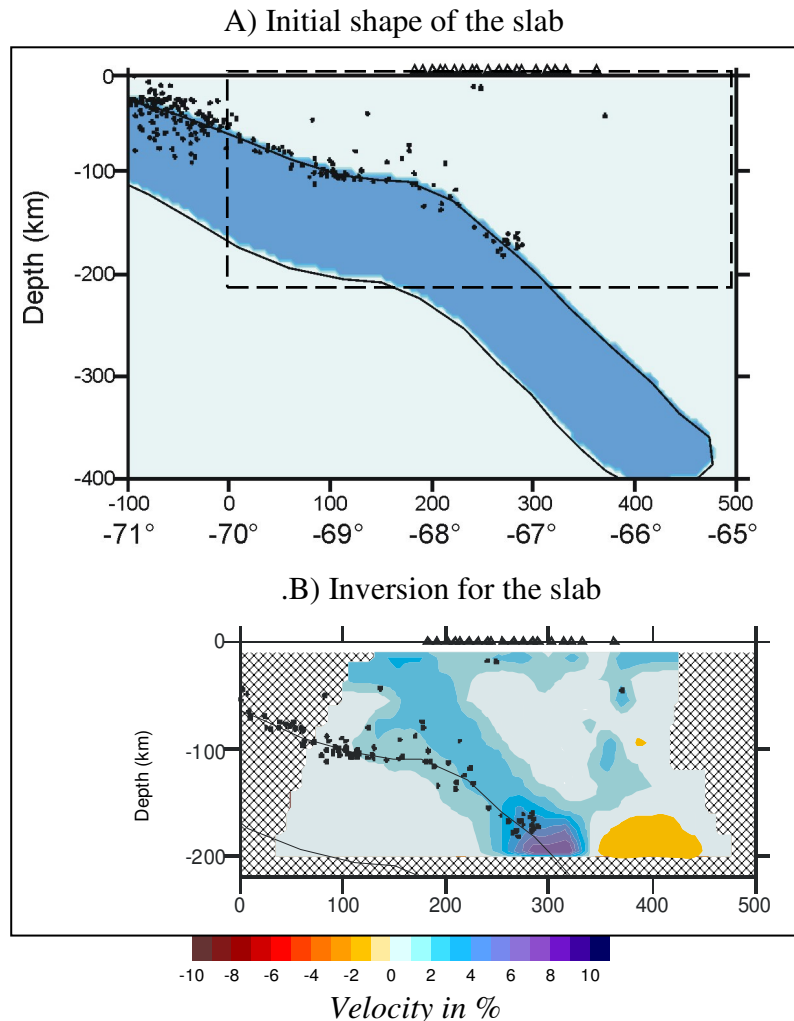


Figure 3.13: A) Initial shape of the slab. Note that this is carried out for a slab down to 400 km depth while the inversion of the data is performed to 200 km depth. The anomaly of the slab is +6%. Triangles represent the stations along the Puna profile. B) Inversion showing results after correcting for the slab.

As shown in Figure 3.13, the inversion after corrections for the slab is performed for a velocity contrast of 6% for the slab anomaly. The initial model and position of the slab is shown in the way that  $dt^{slab}$  are computed along the ray paths down to the depth of 400 km while the inversion is performed for the depth interval 0-200 km. This fact enables the plotting of the slab so that the

upwards shift is not too strong in our study area. It must be observed that this produces an undesired effect that can be seen in the concentration of rays at the bottom of the slab (where it becomes nearly vertical). This effect is usually represented by the development of low-velocity anomalies near the high-velocity end of the slab, as seen in figure 3.13 B at a depth of ~200 km.

### 3.3.2. Real data inversion: Puna

The inversion results for the initially observed residuals are performed along the profile at 25.5°S. The Argentine Puna profile is relatively short (~200 km), with the depth of investigation, according to the incident rays tracing, reaching 200 km. Below this depth we lack the necessary resolution with smearing tending to be larger (Figure 3.14). We have also the chance to compare our results with those from other seismological projects such as PUNA 97 (Schurr et al., 1999 and Schurr, 2000) in the north of our study area.

#### P-velocity anomalies

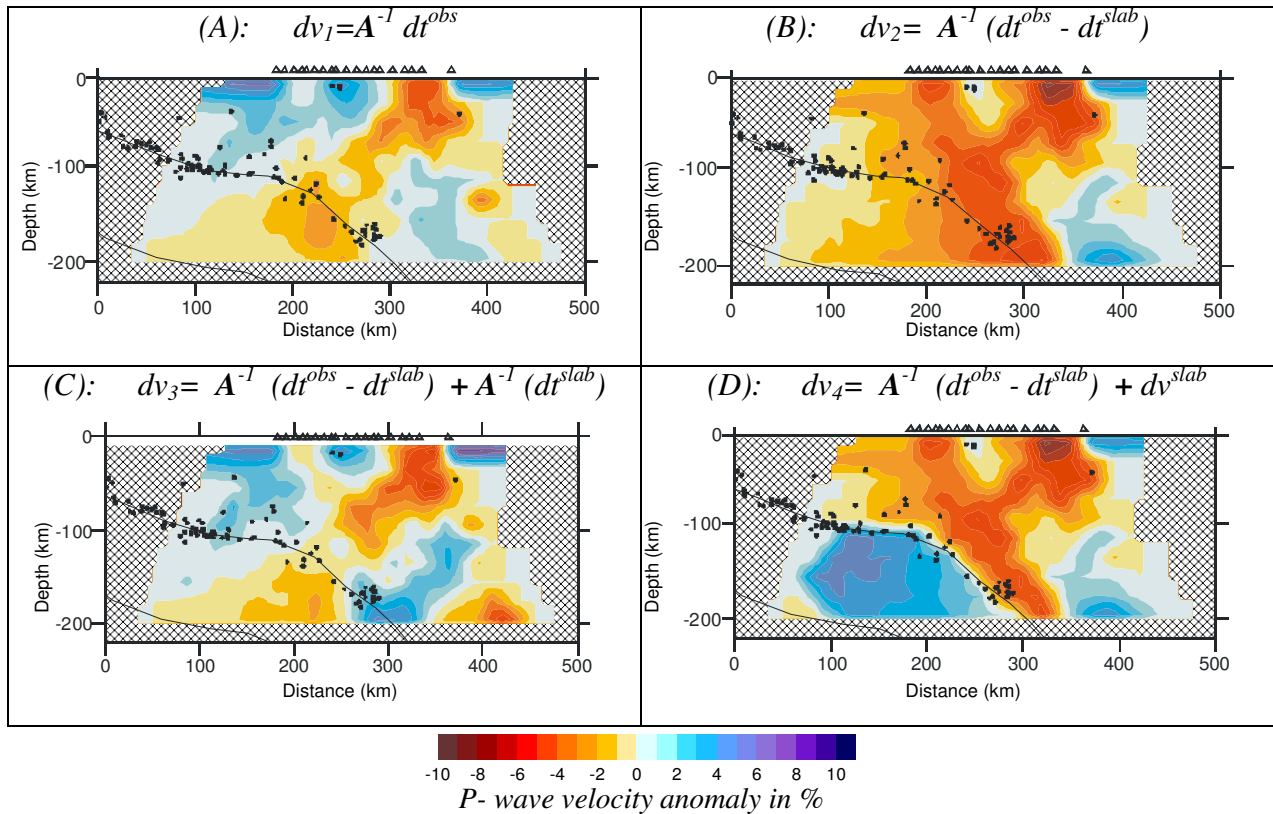


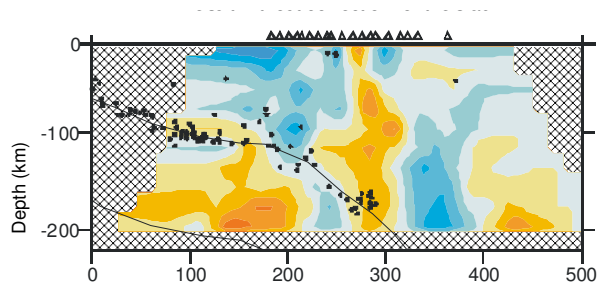
Figure 3.14: Results of the inversion for P- wave residuals with and without information about the slab in three vertical sections. (A): 1-D model inversion without the slab, (B): Inversion for data after the subtraction of the slab, (C): Superposition of the inversion results for “no-slab” residuals with the addition of slab residuals. The models A and C are equivalent when explaining the observed residuals, but C contains a-priori information about the slab. (D): Final section showing the combination of inversion results for “no-slab” residuals with the model of the slab.

The real data inversion results for the Puna profile are shown in Figure 3.14. The model presented in Figure 3.14D:  $dv_4 = A^{-1} (dt^{obs} - dt^{slab}) + dv^{slab}$  is preferred for our interpretation as the image resolves the position of the slab.

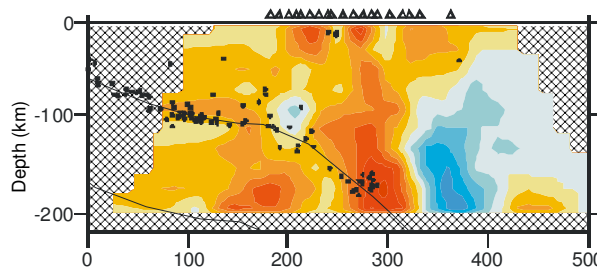
The same strategy as discussed in section 3.2. was applied for the inversion of the S-wave data. The total number of S-wave residuals was about 300, compared to the P-wave data set of 1100 rays. The results are shown in Figure 3.15A, 3.15B and 3.15C. Results for inversion with and without subtraction of the slab are presented. One image is not being displayed (case presented in Figure 3.14C for P-waves). In the initial model, a slab with the velocity contrast of 4% is used. The inversion results for the Puna are presented as horizontal sections in the Appendix A.5.

### S- velocity anomalies

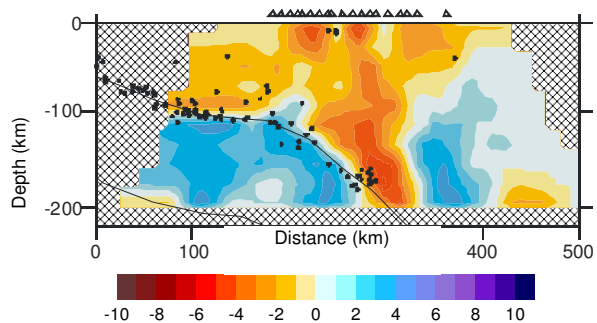
(A):  $dv = A^{-1} dt^{obs}$



(B)  $dv = A^{-1} (dt^{obs} - dt^{slab})$



(C)  $dv = A^{-1} (dt^{obs} - dt^{slab}) + dv^{slab}$



S- wave velocity anomaly in %

Figure 3.15: Results showing the inversion for S-residuals, with and without the slab on vertical sections using the same strategy as in Figure 3.14. Triangles represent the stations.